Behaviour and constitutive modelling of ductile damage of Ti-6Al-1.5Cr-2.5Mo-0.5Fe-0.3Si alloy under hot tensile deformation

Junling Li[a], Baoyu Wang[a,*], He Huang[a], Shuang Fang[b], Ping Chen[a], Jie Zhao[c], Yi Qin[c]

[a] *School of Mechanical Engineering, University of Science and Technology Beijing, Beijing 100083, China*

[b] *Beijing Institute of Aeronautical Materials, Beijing 100095, China*

[c] *Centre for Precision Manufacturing, DMEM, The University of Strathclyde, Glasgow, UK*

*Corresponding author: Baoyu Wang

E-mail address: bywang@ustb.edu.cn (Baoyu Wang), jlli@xs.ustb.edu.cn (Junling Li)

Tel.: +86 10 82375671

Fax.: +86 10 62332923

Postal address: No.30 Xueyuan Road, Haidian District, Beijing 100083, China

Abstract In this paper, the flow softening and ductile damage of TC6 alloy were investigated using a uniaxial hot tensile test with deformation temperatures of 910 °C~970 °C and strain rates of 0.01 s^{-1}~10 s^{-1}. Scanning electron microscopy (SEM) was performed on the deformed specimens to reveal the damage mechanism. The results showed that the flow stress rapidly increases to a peak at a tiny strain, followed by a significant decrease due to flow softening and ductile damage. The ductile damage of the studied TC6 alloy can be ascribe to the nucleation, growth and coalescence of microdefects, and the microvoids preferentially nucleate at the interface of the alpha phase and beta matrix due to the inconsistent strain. Then, a set of unified viscoplastic constitutive equations including flow softening and ductile damage mechanisms was developed and determined, and this set of equations was verified by the experimental flow stress, which indicated the reliability of the prediction. Furthermore, the predicted normalized dislocation density and the adiabatic temperature rise increase with decreasing temperature and increasing strain rate. The predicted damage components show that the microdefects mainly nucleate in the initial stage, but then primarily grow

and link together with continuing deformation.

Keywords: ductile damage, flow behaviour, titanium alloy, unified constitutive model, micro defects, nucleation

1 Introduction

Titanium and its alloys have been widely used in aircraft and automotive engines due to their superior specific strength, high operating temperature and corrosion resistance. Plastic forming processes, such as forging, hot stamping and extrusion, are the dominant and effective technologies used to manufacture titanium alloy components[1]. However, the microstructure and mechanical properties of titanium alloys are very sensitive to the deformation parameters during the high-temperature plastic forming, and combined with their lower thermal conductivity and larger deformation heating, the forming window of titanium alloys has been limited[2, 3]. Consequently, the principal considerations of relevant research are the influence of deformation parameters on the flow behaviour and microstructure evolution. A number of works on the flow behavior and microstructure evolution associated with constitutive modelling have been performed[3-8]. Bai et al.[9] proposed a set of unified elastic-viscoplastic constitutive equations based on mechanisms to model the flow softening of Ti-6Al-4V alloy. The mechanisms of globularisation induced by beta strain, dislocation evolution, and adiabatic heating were considered. Huang et al.[10] characterized the dynamic recrystallization (DRX), flow instability and texture of compressed Ti-6.5Al-3.5Mo-1.5Zr-0.3Si alloy with an equiaxed microstructure. They found that the DRX decreases the fraction of low angle boundaries (LABs) and increases the fraction of high angle boundaries (HABs). Luo et al.[11]investigated the effects of processing parameters on the flow stress, the strain rate sensitivity and the strain hardening exponent of TC18 alloy. The results showed that thermal and microstructure-related softening are competing with the work hardening to control flow behaviour. Gao et al.[12] studied the flow behaviour and microstructure evolution of TA15 alloy with a nonuniform microstructure consisting of equaxied and lamellar α phase. The results showed that the lamellar α phase undertakes most of the deformation and turns to be bended and globularized, inducing the higher softening rate than equaxied α phase.

Ductile fracture is another increasingly important issue during the high-temperature plastic forming of titanium alloy. The most important area in which our knowledge of ductile fracture is the macroscopic consequence of the nucleation, growth and coalescence of the micro defects, such as voids and cracks[13-16]. Semiatin et al.[17, 18]investigated the cavitation during hot tension testing of Ti-6Al-4V alloy with several different types of transformed beta phase, and the results showed that the cavity initiation occurred due to an obvious mismatch deformation. Dong et al.[19] investigated the cavity nucleation of Ti-6Al-2Zr-1Mo-1V alloy with the colony alpha microstructure using the isothermal hot compression test. The results showed that most of the cavities nucleated along the prior beta phase boundaries, and the increase of the volume fraction of the beta phase helps to inhibit cavity nucleation. Nicolaou et al. [20] proposed that the cavity initiation sites are different within notch of different sizes, due to the difference in local stress states, and the cavity growth rate was also correlated to the stress state. The effect of the strain rate and stress triaxiality on the tensile behaviour of Ti-10V-2Fe-3Al alloy at were also investigated by Bobbili et al. [21].

One of the most difficult tasks encountered in well documenting the damage behaviour and underlying mechanism is to develop dependable models for accurately simulation and predication. Historically, Cockcroft and Latham developed an empirical damage criterion based on the energy accumulation theory (C-L model), which recognizes that the fracture occurs once when the maximum tensile stress reaches a threshold[22]. Then, this criterion was modified by Brozzo et al.[23], in which the hydrostatic pressure was introduced. Likewise, Johnson-Cook (J-C model)[24], McClintock[25], Oyane[26] and Rice and Tracey[27] successively proposed damage criteria. These phenomenological damage models have been increasingly applied to fracture prediction in the bulk forming due to their easy implementation in the commercial finite element (FE) software as well as the parameter identification. A further framework for damage prediction is the porosity model, whose foundation is based on the micromechanics concepts. The Gurson model, proposed by Gurson[28], is a typical representation, in which a plastic potential equation to describe the effect of the damage holes was developed. However, the hole size and the spacing between the holes were not taken into account. Therefore, Tvergaard and Needleman et al.[29, 30] improved the predictive accuracy by substituting the porosity with a variable, and the improved models came to be known of as GTN models.

The aforementioned damage models have been widely used due to their simplicity. However, the simplicity brings about the shortcomings. The big issue is the uncoupling of damage and plasticity, which means that the effect of damage cannon be transiently and continuously fed back to the plastic deformation. Therefore, the continuum damage mechanics (CDM) have received ever-increasing attention. Much research has been carried out to develop the CDM models and understand microscopic fracture behaviour. Hayhurst et al.[31] investigated the creep fracture of a welding part at high temperature, and established the relationship between the damage internal variable and creep strain rate. Lin et al.[32] developed a set of generalized constitutive equations to reveal the nucleation and growth of the damage. This set of equations has been successfully applied to many types of materials[33-35]. Huo et al.[33] developed a multiaxial constitutive model coupling the microstructure and ductile damage of a high-speed railway axle steel during cross wedge rolling, the result showed that the developed model can reliably predict the grain size and ductile damage evolution. Xiao et al.[34] studied the flow behaviour and ductile damage of AA7075 aluminium alloy by developing a constitutive model coupled with the evolution of dynamic crystallization, grain size and damage. Yang et al.[35] formulated a set of constitutive equations to investigate the underlying mechanism of flow softening and ductile damage of TA15 titanium alloy in sheet forming.

The above discussion provides an insight into the investigation of ductile fracture behaviour and damage modelling. In this study, hot tensile tests for TC6 alloy, which is a desirable material for the blade of aviation engines, were carried out to investigate the flow behaviour, and SEM was performed on the deformed specimens to observe the fracture surface morphology and deformed microstructure. A set of constitutive equations coupling ductile damage, dislocation density, flow softening induced by adiabatic temperature rise and phase transformation, was developed, determined and verified. Afterward, the evolution of the internal variables, such as the dislocation density, adiabatic temperature rise, damage component and damage factor, was predicted and analysed.

2 Experimental details

2.1 Materials

The titanium TC6 alloy used in the present study was supplied by Baotai Group Co., Ltd. Its nominal composition is Ti-6Al-1.5Cr-2.5Mo-0.5Fe-0.3Si. The initial microstructure is shown in Fig.1. There are lath and equiaxed primary alpha phases and acicular transformed beta phase dispersed throughout the matrix. The finial transformation temperature of the alpha to beta phase is 985 °C[36].

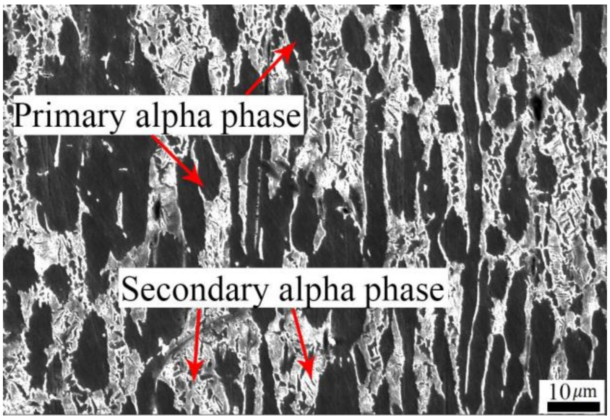

Fig. 1 Initial microstructure of the studied TC6 alloy.

2.2 Uniaxial hot tensile tests

Uniaxial hot tensile tests were conducted on a Gleeble-3500D thermal simulation machine. The specimens used in the tests were manufactured by wire-electrode cutting. Fig. 2a and Fig. 2b show the dimensions of the specimens and the experimental route, respectively. The specimens were first heated at a rate of 10 °C s^{-1} to the predetermined temperature and held at that temperature for 3 min to obtain a balanced temperature distribution. Then, the specimens were stretched at different strain rates until fracture occurred. The deformed specimens were forced-air quenched immediately to freeze the deformed microstructure. Load-displacement curves were automatically recorded to derive the true stress-strain curves.

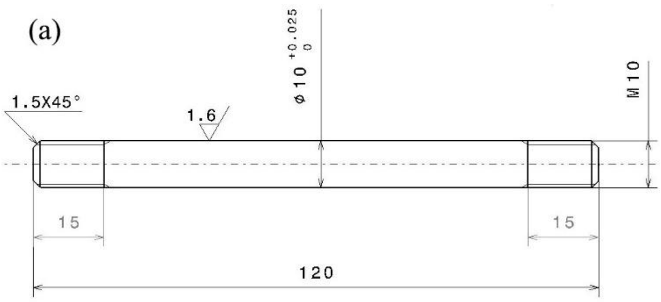

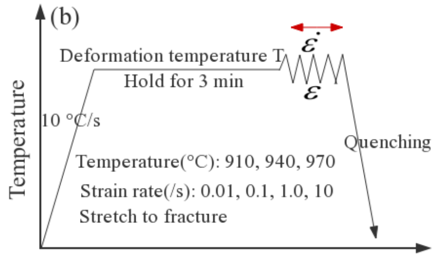

Fig. 2 Schematic diagrams of (a) a tensile sample and (b) the tensile test process

2.3 Metallographic examination

After cooling, the fracture surface was carefully taken from the deformed specimen and ultrasonically cleaned, and comprehensively inspected by SEM to discriminate the fracture morphology. SEM examination of the cross-section close to the fracture surface was also performed to disclose the micro damage mechanism. All the cross-sections were subjected to standard metallurgical processing and then etched with Kroll solution (HF: HNO_3: H_2O= 1: 2: 50)[36].

3 Deformation mechanisms

3.1 True stress-train curves

Fig. 3 shows the true stress-strain curves, which were calculated from the load-displacement recorded by the hot tensile machine[35]. It is clear that the flow stress decreases with increasing deformation temperature and decreasing strain rate. For all the flow curves, the flow stress first increases up to a peak at a small strain, defined as ε_p , and the values of ε_p are less than 0.05, which indicates the tremendous accumulation of the dislocations. Soon afterwards, the flow stress decreases with the continuation of deformation due to flow softening, and when the specimens undergo necking and finally pulled off, the flow stress instantaneously drops. The strain when fracture occurs is called the failure strain ε_f . It can be seen from Fig. 3 that the values of ε_f increase with increasing the deformation temperature and decreasing the strain rate, similar to the flow stress.

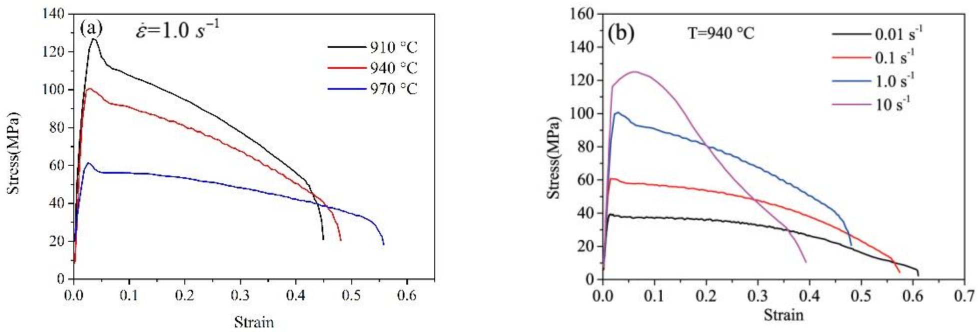

Fig. 3 True stress-strain curves of the studied TC6 alloy under the deformation

conditions of (a) $\dot{\varepsilon}=1.0\,s^{-1}$ and (b) $T=940\,°C$.

3.2 Flow softening mechanism

The accumulation of dislocations, as aforementioned, contributes to the work hardening (WH) through continuous slipping and climbing, leading to a very rapid increase in the flow stress. In contrast, the flow softening caused by the rearrangement and annihilation of the tangled dislocations induces a reduction of the flow stress. Many deformation mechanisms are attributed to the flow softening, such as dynamic recovery (DRV) and DRX. For the studied TC6 alloy, no DRX was evident due to the initial microstructure[37]. However, it has been reported that adiabatic temperature rise and phase transformation from the harder alpha phase to the beta phase also contribute to the flow softening.

The flow softening caused by adiabatic temperature rise is also known as thermal softening. The heat generated by the plastic deformation is trapped within the specimen rather than easily dissipated, leading to an increase in the transient temperature and softening of the stress response. Furthermore, the increasing temperature also lowers the mobility barrier of dislocations and changes the microstructure.

As a two-phase titanium alloy, TC6 alloy exhibits two crystal structures, and the variation of temperature enables their mutual conversion, i.e., the hexagonal close-packed (*hcp*) alpha phase at lower temperature and the body-centred cubic (*bcc*) beta phase at higher temperature. Because the *bcc* beta phase itself has more slip systems and better crystal plasticity, the proportion of each phase affects the stress response[9].

Fig. 4 shows the comparison of the hot compressive and hot tensile curves at a deformation temperature of 940 °C and a strain rate of 10 s^{-1}. The flow stress will be restricted if the WH is counterbalanced by DRV (dashed line)[38]. However, the flow stress follows the red line if the aforementioned softening mechanism is triggered and contributes to the reduction of flow stress $\Delta\sigma_1$ under compression. In the tension state, the flow stress decreases $\Delta\sigma_2$ can be ascribed to the ductile damage, which reduces the effective pressure bearing area as well as the applied loading. Therefore, the total reduction of flow stress $\Delta\sigma$ in tensile tests can be formulated as $\Delta\sigma=\Delta\sigma_1+\Delta\sigma_2$.

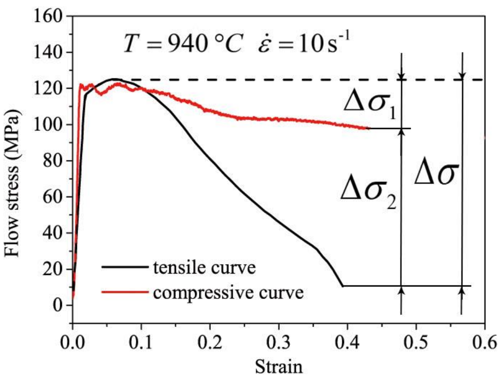

Fig. 4 Typical flow curves during hot tensile and compressive tests.

3.3 Fractography and damage mechanisms analysis

3.3.1 Fractography analysis

The fracture surface morphologies of the deformed specimen obtained under different conditions are shown in Fig. 5. All of the fracture surfaces are fully coved by dimples and voids, which are the general characteristics of ductile damage[39]. Apart from the preexisting voids, the nucleated dimples and voids grow up due to large plastic deformation, and then, the dimples and voids with larger enough diameters tend to link together and coalesce to form microcracks, which eventually leads to material fracture or bearing failure[40]. The nucleation and growth of the dimples and voids are significantly affected by the deformation parameters. At the lower deformation temperature and lower strain rate, as shown in Fig. 5a, fewer dimples and holes exist, and some of these ductile dimples exhibit a larger diameter. However, the amount of the ductile dimples increases with increasing the strain rate to 1.0 s^{-1}, and the ductile dimples become shallower without further growth. When the deformation temperature increases to 940 °C, the amount of the ductile dimples decreases, but the dimples grow deeper. Thus, the nucleation rate of the ductile dimples increases with increasing the strain rate and decreasing the deformation temperature, as does the coalescence rate of the ductile dimples.

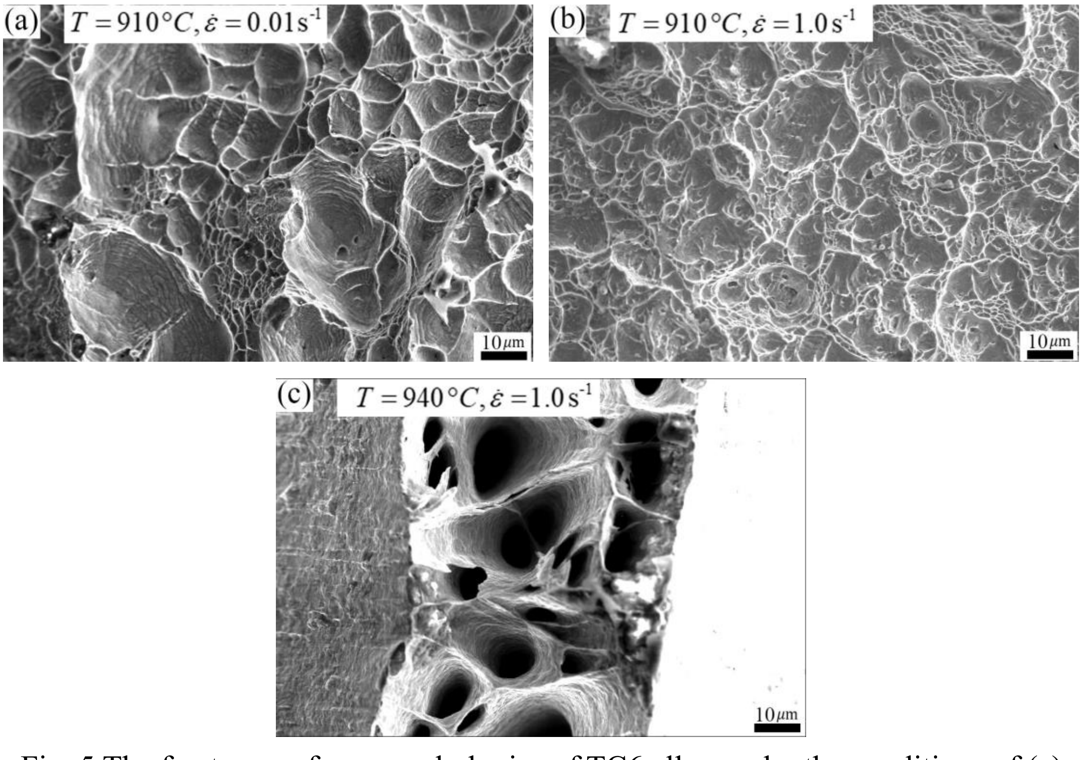

Fig. 5 The fracture surface morphologies of TC6 alloy under the conditions of (a) $T=910\,°C, \dot{\varepsilon}=0.01s^{-1}$; (b) $T=910°C, \dot{\varepsilon}=1.0s^{-1}$; and (c) $T=940°C, \dot{\varepsilon}=1.0s^{-1}$.

3.3.2 Damage mechanisms analysis

Fig. 6 shows the SEM images of the micro voids and cracks on the cross-section located close to the fracture surface of deformed specimens. The majority of the voids nucleate at the interface of the grain boundary of the equiaxed alpha phase and the surrounding matrix, and a few initiate in the softer, ductile beta matrix. During the deformation, the microvoids are pulled and stretched to grow and link together and finally transform into microcracks. Furthermore, the coalesced cracks link the adjacent equiaxed alpha phase along the shortest path, or intersect with other cracks to form the triangular cracks. The directions of the growth, coalescence and intersection of the micro voids and cracks are in accordance with the stretching direction.

As a two-phase titanium alloy, TC6 alloy exhibits cooperative and competitive coexistence of the *hcp* alpha phase and *bcc* beta phase, as mentioned above. When the applied stress and strain concentrates at the interface of the alpha phase and beta matrix, the inconsistent strain provides a nucleation site for voids. Therefore, it can be deduced that the cavities preferentially nucleate at the interface of the alpha phase and beta matrix, and similar conclusions have been reported by Seminatin et al.[18]and Dong et al.[19]. Based on the microstructure examination, it is worth noting that more serrated microcracks appeared in the specimen deformed under higher temperature. The mechanisms involved have not been reported up to now, so further research is needed.

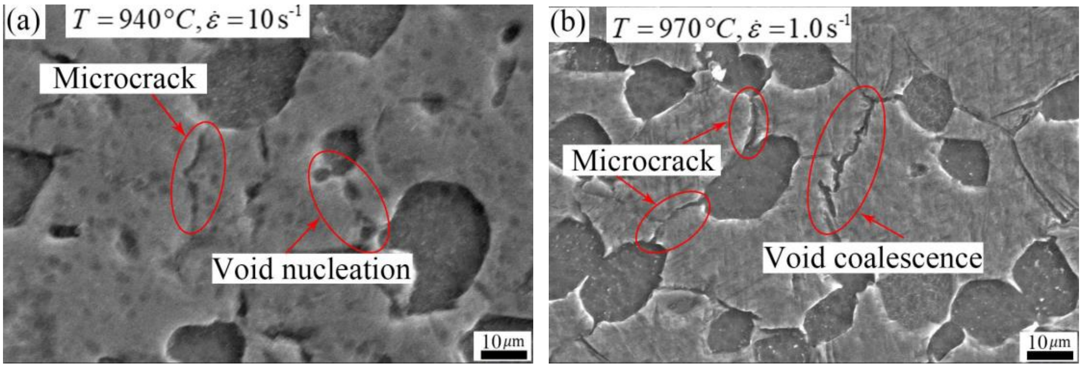

Fig. 6 SEM images of the micro voids and cracks on the deformed specimens.

4 Constitutive modelling

4.1 Damage evolution

The damage mechanism of the studied TC6 alloy involves void nucleation, growth and coalescence to form microcracks. Let D be the damage variable, which is formulated as follows [41]:

$$D = \frac{A - \tilde{A}}{A} \quad (1)$$

where A is the total resisting area defined by the normal direction of the applied load, and $\tilde{A}$ is the effective resisting area during the deformation. In the studied uniaxial hot tensile tests, the damage variable D can be defined as a scalar. From a mathematical point of view, D increases from 0 (corresponding to the undamaged state) to 1 (corresponding to the fracture state). However, the material is considered to fail when the value of D reaches a threshold, and the threshold is taken to be 0.7 in this study[13, 35].

It has been reported that the damage evolution is greatly affected by the flow stress, strain rate and strain and other variables during hot-working processes as $\dot{D}=f(\sigma,\dot{\varepsilon}_p,\varepsilon\cdots)$. Moreover, the damage mechanism of the studied TC6 alloy is very similar to what occurs in the works of Semiatin et al.[18], Lin et al.[13, 42], and Yang et al.[35]. Therefore, the damage model proposed by Lin et al.[13] is adopted. As a handful of the voids directly nucleates in the beta matrix due to the concentration of stress and strain, so the model has been modified as follows:

$$D=D_{nucleation}+D_{growth} \tag{2}$$

$$\dot{D}_{nucleation}=\beta_1(1-D)\left|\dot{\varepsilon}_{p,\alpha}-\dot{\varepsilon}_{p,\beta}\right|^{\beta_2}\sigma^{\beta_3} \tag{3}$$

$$\dot{D}_{growth}=\frac{\beta_4\cosh\left(\beta_5\varepsilon_p\right)\dot{\varepsilon}_p{}^{\beta_6}}{\left(1-D\right)^{\beta_7}} \tag{4}$$

where $\dot{D}_{nucleation}$ and $\dot{D}_{growth}$ represent the void nucleation and void growth rates, respectively. β_1 and β_4 are the temperature dependent parameters that control the rates of nucleation and growth from the overall perspective. β_2 and β_3 correspond to the effects of inconsistent strain and flow stress, respectively. β_5 is a temperature-dependent parameter that adjusts the growth of voids with increasing deformation strain. The temperature dependent parameter β_6 represents the effect of the applied strain rate on the growth of voids. β_7 restricts the ε_f to less than the threshold.

4.2 Flow softening evolution

Based on the aforementioned discussion, the flow softening of the studied TC6 alloy can be ascribed to adiabatic temperature rise and phase transformation, which can be formulated as follows[9, 13]:

$$\dot{T}_\varepsilon=\eta\frac{\sigma}{cd}\left|\dot{\varepsilon}_p\right| \tag{5}$$

$$\dot{f}_\beta=\mu_1\left(\frac{f_\beta}{0.5}\right)^{\mu_2}(1-f_\beta)^{\mu_3}\dot{T}_\varepsilon \tag{6}$$

where T_ε represents the adiabatic temperature rise converted from the deformation energy and η is the conversion coefficient. *c* and *d* are the specific heat and material density, respectively. In Eq. (6), f_β represents the volume fraction of beta phase, μ_1,

μ_2 and μ_3 are material constants determined by the phase transformation test, and the corresponding details about the test procedure and results are described elsewhere[36].

4.3 Plastic flow rule

Generally, the overall flow stress can be divided into the initial yield stress, WH stress and viscoplastic stress:

$$\sigma = k + H + \sigma_v \tag{7}$$

where $\sigma\left(MPa\right)$ is the total flow stress, k $\left(MPa\right)$ is the initial yield stress, H $\left(MPa\right)$ is the WH stress and σ_v $\left(MPa\right)$ is the viscoplastic stress.

According to the Norton's law $\dot{\varepsilon}_p = (\sigma_v / \lambda^*)^{N^*}$, the flow rule of the material can be described as Eq. (8):

$$\dot{\varepsilon}_p = \left\langle \frac{\sigma - k - H}{K} \right\rangle^n \tag{8}$$

where $\dot{\varepsilon}_p$ $\left(s^{-1}\right)$ is the plastic strain rate, K is a temperature-dependent parameter, n is the viscosity exponent. $\langle\ \rangle$ represents the Macaulay brackets, which means that the term is inapplicable only when the plastic deformation occurs.

Concerning TC6 alloy, a typical two-phase titanium alloy, the plastic strain rate can be decomposed into two parts, the plastic strain rates of the alpha and beta phases, as shown below[9, 35]:

$$\dot{\varepsilon}_p = \dot{\varepsilon}_{p,\alpha}(1 - f_\beta) + \dot{\varepsilon}_{p,\beta} f_\beta \tag{9}$$

where $\dot{\varepsilon}_{p,\alpha}$ and $\dot{\varepsilon}_{p,\beta}$ are the plastic strain rates of the alpha and beta phases, respectively. During the hot tensile deformation, the side effect of ductile damage on the total flow stress needs to be considered. Then, the flow rule is rewritten as follows:

$$\dot{\varepsilon}_{p,\alpha} = \left\langle \frac{\sigma / (1 - \mathrm{D}) - k_\alpha - H}{K_\alpha} \right\rangle^n \tag{10}$$

$$\dot{\varepsilon}_{p,\beta} = \left\langle \frac{\sigma / (1 - \mathrm{D}) - k_\beta - H}{K_\beta} \right\rangle^n \tag{11}$$

where k_α and k_β are the initial yield stresses of the alpha and beta phases, respectively, and they are temperature dependent and decrease with increasing temperature. K_α and K_β are also temperature-dependent parameters that decrease with increasing temperature.

According to Hooke's law, the total flow stress of a material under hot tensile deformation is calculated by[34]:

$$\sigma = (1\text{-D})E(\varepsilon_T - \varepsilon_p) \tag{12}$$

where ε_T denotes the total strain, and E represents the intrinsic Young's modulus of the material, which is a temperature-dependent parameter that decreases with increasing temperature.

4.4 Dislocation density evolution

Under the hot tensile conditions, the material is subjected to high temperature and plastic deformation accompanied by the evolution of the dislocation density. Various deformation mechanisms are involved. The generation of the new dislocation and their climbing with the existing dislocations causes the multiplication of dislocations and working hardening. Meanwhile, the stored energy of the material enhances and drives the recovery and microstructure change. Conversely, the recovery, including the statics and dynamics recovery, leads to absorption of the tangled dislocations, causing the annihilation of dislocation. Bai et al.[9]and Yang et al.[35] formulated the evolution of the dislocation density as Eq. (13). To adjust for the effect of the plastic strain rate, a controlled coefficient δ_1 was introduced, as Eq. (14) shows:

$$\dot{\bar{\rho}} = A(1-\bar{\rho})\left|\dot{\varepsilon}_p\right| - C\bar{\rho}^{\delta} \tag{13}$$

$$\dot{\bar{\rho}} = A(1-\bar{\rho})\left|\dot{\varepsilon}_p\right|^{\delta_1} - C\bar{\rho}^{\delta} \tag{14}$$

where $\dot{\bar{\rho}}$ is the evolution rate of normalized dislocation density. And A and C are temperature-dependent parameters that decrease with decreasing temperature. δ is material parameter that controls the effect of static recovery.

The isotropic WH is closely related to the accumulation and annihilation of dislocations, therefore, it is formulated as shown below [33]:

$$H = B\bar{\rho}^{0.5} \tag{15}$$

where $\bar{\rho}$ is the normalized dislocation density. B is a temperature-dependent parameter that decreases with increasing temperature.

The aforementioned temperature-dependent parameters are summarized in Table 1, and all of them are formulated in Arrhenius relations based on their variation tendency with the deformation temperature. In Table 1, R is the universal gas constant which equals to 8.3145 $J \bullet mol^{-1} \bullet K^{-1}$, and T is the absolute temperature in K.

Table 1 List of temperature dependent parameters.

$k_\alpha = k_{\alpha,0}\exp(Q_k/RT)$	$K_\alpha = K_{\alpha,0}\exp(Q_K/RT)$	$n = n_0\exp(Q_n/RT)$
$E = E_0\exp(Q_E/RT)$	$B = B_0\exp(Q_B/RT)$	$A = A_0\exp(-Q_A/RT)$
$C = C_0\exp(-Q_C/RT)$	$\beta_1 = \beta_{1,0}\exp(Q_1/RT)$	$\beta_4 = \beta_{4,0}\exp(Q_4/RT)$
$\beta_5 = \beta_{5,0}\exp(Q_5/RT)$	$\beta_6 = \beta_{6,0}\exp(Q_6/RT)$	$\beta_7 = \beta_{7,0}\exp(Q_7/RT)$

5 Results and discussions

5.1 Determination of material constants

Two steps are required to determine the material constants. However, the phase transformation process is identical to that in the test that has already been carried out by the author due to the consistency of the experimental material[36]. Therefore, the material constants μ_1, μ_2 and μ_3 were employed in the present study. The next step is to determine the rest of the parameters based on the experimental stress-strain flow curves. An optimization method based on a genetic algorithm (GA) in MATLAB software was adopted by minimizing the residuals between the experimental and computed values. The details of the optimization process have been described by elsewhere[42]. The determined material constants are listed in Table 2.

Table 2 Determined values of material constants

Material constants	Optimal value	Material constants	Optimal value
$k_{\alpha,0}$ (MPa)	9.7803E-4	Q_k ($J \bullet mol^{-1}$)	9.1160E4
$K_{\alpha,0}$ (MPa)	8.2681E-2	Q_K ($J \bullet mol^{-1}$)	6.5647E4
E_0 (-)	4.0811E3	Q_E ($J \bullet mol^{-1}$)	5.0858E3
B_0 (MPa)	1.0173E0	Q_B ($J \bullet mol^{-1}$)	4.2972E4
A_0 (-)	6.8775E2	Q_A ($J \bullet mol^{-1}$)	5.1523E4
C_0 (-)	2.7851E17	Q_C ($J \bullet mol^{-1}$)	3.4876E5
$\beta_{1,0}$ (-)	2.0196E-3	Q_{β_1} ($J \bullet mol^{-1}$)	7.0475E4
$\beta_{4,0}$ (-)	1.348E-2	Q_{β_4} ($J \bullet mol^{-1}$)	4.6921E4
$\beta_{5,0}$ (-)	1.2870E-1	Q_{β_5} ($J \bullet mol^{-1}$)	3.4987E4
$\beta_{6,0}$ (-)	4.1143E-1	Q_{β_6} ($J \bullet mol^{-1}$)	3.4948E4

$\beta_{7,0}$ (-)	2.5203E-2	Q_{β_7} ($J \bullet mol^{-1}$)	1.3485E4
δ (-)	1.1265	δ_1 (-)	4.6923
η (-)	0.9558	β_2 (-)	1.5598
β_3 (-)	5.0182		

5.2 Validation of the constitutive equations

Fig. 7 shows the comparison of the flow stress between the experimental (symbol) and computed (line) results under different deformation temperatures. The deformation mechanisms, including WH, flow softening and ductile damage, can be satisfactorily predicted. Most of the experimental values are close to the computed line, which indicates a good prediction of the developed constitutive model.

To evaluate the degree of linear correlation of the proposed constitutive equations, some indexes for statistical analysis, including the correlation coefficient (R), the average absolute relative error ($AARE$) and the root mean square error ($RMSE$), were calculated as:

$$R=\frac{\sum_{i=1}^{N}(\mathrm{E}_i-\bar{E})(P_i-\bar{P})}{\sqrt{\sum_{i=1}^{N}(\mathrm{E}_i-\bar{E})^2\sum_{i=1}^{N}(P_i-\bar{P})^2}} \tag{16}$$

$$AARE=\frac{1}{N}\sum_{i=1}^{N}\left|\frac{E_i-P_i}{E_i}\right|\times 100\% \tag{17}$$

$$RMSE=\sqrt{\frac{1}{N}\sum_{i=1}^{N}(\mathrm{E}_i-P_i)^2} \tag{18}$$

where E_i and $\bar{E}$ are the experimental stress and average experimental stress, respectively. P_i and $\bar{P}$ are the computed stress and average computed stress predicted by the developed constitutive model, respectively. N is the total number of the calculated points. Fig. 8 shows the best linear fitting between the experimental and computed stresses at different deformation temperatures and strain rates. It can be seen that the R is very close to 1.0, and the maximum values of $AARE$ and $RMSE$ are 5.4986% and 3.1572%, respectively, which manifests the developed model has a good forecasting capability.

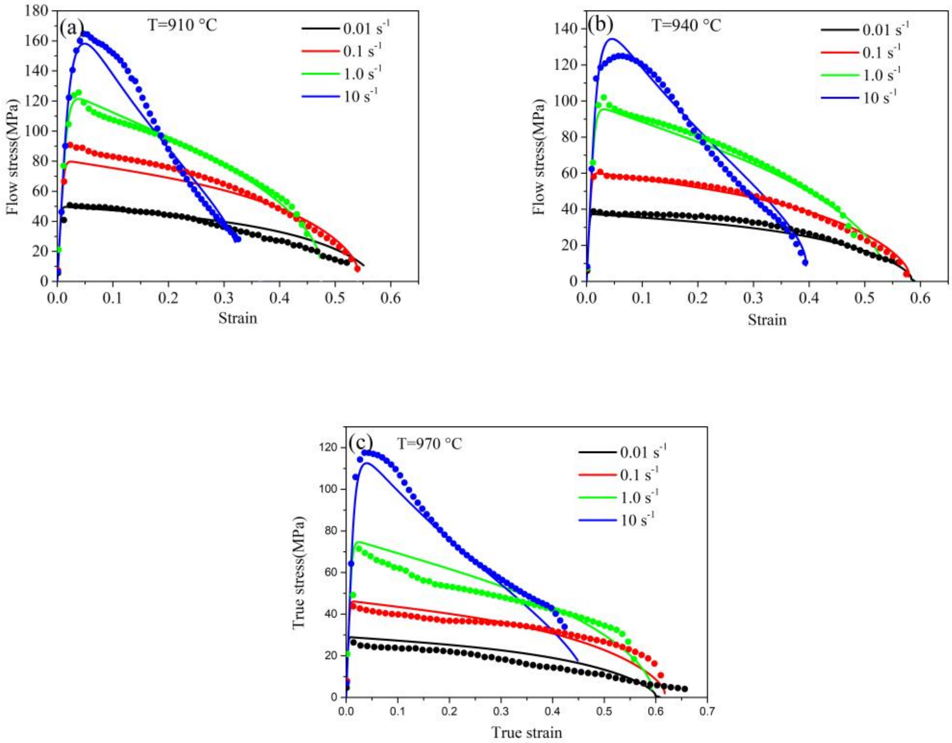

Fig.7 Comparison of the experimental (symbol) and computed (line) stress data at different deformation temperatures of (a) $T=910°C$, (b) $T=940°C$ and (c) $T=970°C$.

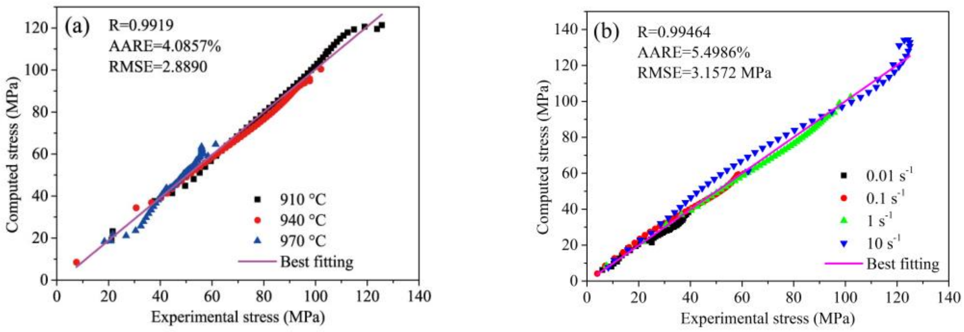

Fig. 8 Correlation between the experimental and computed stresses at different deformation conditions of (a) $\dot{\varepsilon}=1.0s^{-1}$ and (b) $T=940°C$.

5.3 Evolution of the internal variables

Fig. 9a shows the evolution of the computed normalized dislocation density. The competing processes involved in the evolution of dislocations are accurately predicted. The dislocation density increase sharply in the initial stage of deformation due to the creation and accumulation of dislocations, which causes the WH. Then, it remains stable immediately following a peak, which is attributed to the rearrangement and annihilation of dislocations by the static and dynamic recovery. Overall, the normalized dislocation density increases with decreasing deformation temperature and increasing strain rate.

The evolution of the adiabatic temperature rise under different deformation temperatures and strain rates was shown in Fig. 9b. According to Eq. (10), the adiabatic temperature rise is a function of the flow stress, plastic strain, specific heat capacity and mass density. Therefore, it increases with increasing strain at a given deformation temperature and strain rate. An increase in temperature has a negative effect on changes in the adiabatic temperature rise, but an increase in strain rate exhibits the opposite trend. When the specimen is deformed under the lowest strain rate of 0.01 s^{-1}, the adiabatic temperature rise is very small. These results support the conclusion proposed by Khan et al.[43] that the adiabatic temperature rise has a more significant influence on the specimens deformed under a higher strain rate. Therefore, instead of the adiabatic temperature rise, other softening mechanisms, such as dynamic/statics recovery and phase transformation, are the main reasons for the flow softening when the strain rate is very low.

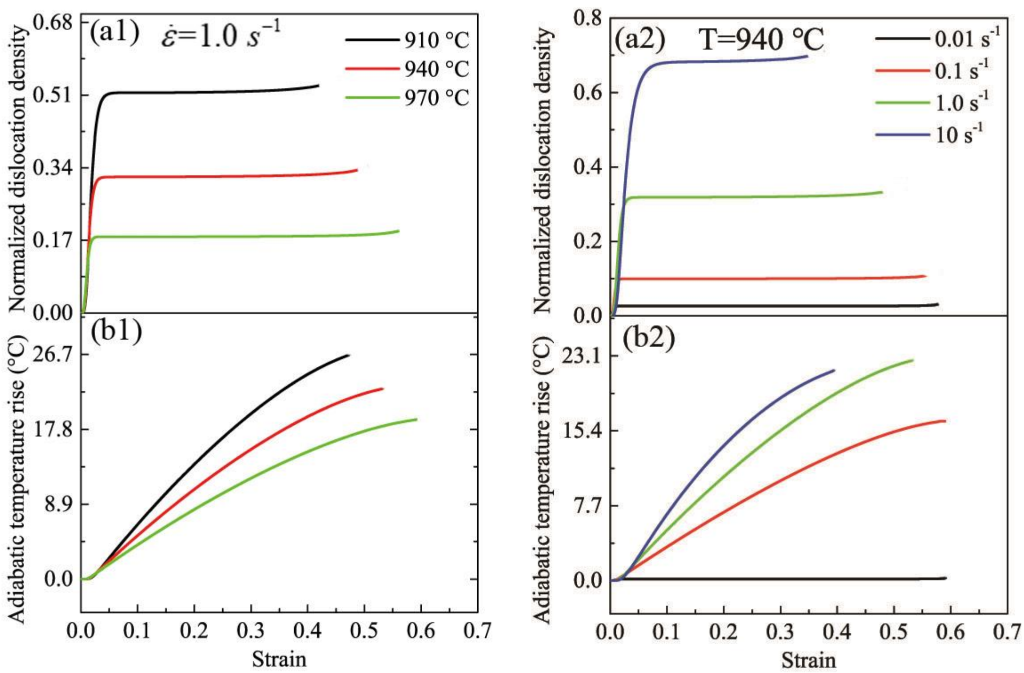

Fig. 9 Predicted evolution of the (a) Normalized dislocation density and (b) adiabatic temperature rise under different deformation temperatures and strain rates.

The ductile damage mechanism of the studied TC6 alloy, under a uniaxial tensile test, is assumed to be the nucleation and growth of micro defects. Notwithstanding, dynamically tracking the relationship between the nucleation and growth of microdefects and stretching strain using precision density measurements or quantitative metallography during the tests is difficult, this relationship can be predicted by the developed constitutive model. Fig. 10 shows the damage components, including nucleation rate and growth rate, and damage factor as a function of the true strain under different conditions. Clearly, the nucleation and growth rates increase with decreasing deformation temperature and increasing strain rate, which is consistent with the fractorgraphy observations. Under a higher strain rate of 1.0 s^{-1}, the nucleation rate increases sharply with strain and then decreases relatively slowly (Fig. 10a1). In contrast, the growth rate achieves a significant rise at a larger strain (Fig. 10b1). This result indicates that the microdefects mainly nucleate in the early stage of deformation, but primarily grow and link together with continuing deformation. The nucleation and growth rates for each strain rate under a deformation temperature of 940 °C vary widely, especially at a lower strain rate of 0.01 s^{-1}. Fig. 10c shows the evolution of the computed total damage factor. Similarly, the damage factor increases with decreasing deformation temperature and increasing strain rate. The damage factor increases linearly from 0 at the initial deformation, which indicates that the material is undamaged. Then, the damage factor exhibits a rapidly increase due to the accumulation of microdefects until the materials fails.

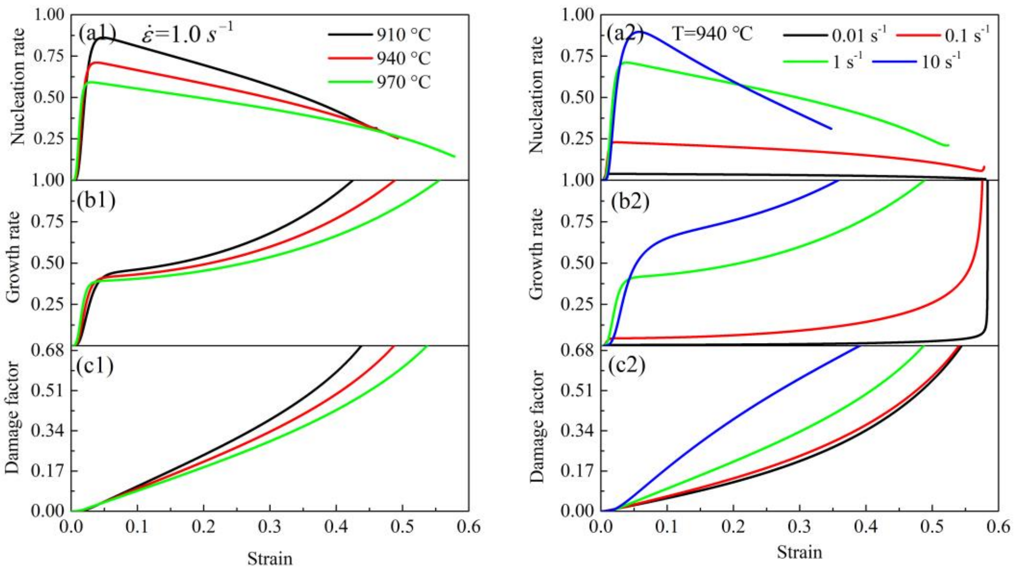

Fig. 10 Prediction of the (a) nucleation rate, (b) growth rate and (c) damage factor under different deformation temperatures and strain rates.

6 Conclusion

(1) The flow softening and ductile damage behaviours of TC6 alloy were investigated under uniaxial hot tensile conditions. The flow stress rapidly increases to a peak at a tiny strain, followed by a decrease in stress due to flow softening and ductile damage.

(2) SEM observations reveal that the ductile damage of the studied TC6 alloy can be ascribed to the nucleation and growth of microdefects. The microvoids preferentially nucleate at the interface of the alpha phase and beta matrix due to the inconsistent strain between the *hcp* alpha phase and *bcc* beta phase.

(3) A set of unified viscoplastic constitutive equations including flow softening and ductile damage mechanisms has been developed, determined and verified. The

computed flow stress agrees well with the experimental data, and the maximum values of *AARE* and *RMSE* are 5.4986% and 3.1572%, respectively, which indicates the reliability of the prediction of the developed model.

(4) The predicted normalized dislocation density increases with decreasing deformation temperature and increasing strain rate. The adiabatic temperature rise has a more significant influence when the specimen is deformed under higher strain rates. The predicted damage components show that the microdefects mainly nucleate in the early stage of deformation but then primarily grow and link together with continuing deformation.

Acknowledgment

This work was supported by the National Natural Science Foundation of China [Grant No. 51505026], and was also supported by the Beijing Laboratory of Modern Transportation Metal Materials and Processing Technology.

Reference

[1]. C. Leyens, M. Peters, Titanium and titanium alloys: Fundamentals and Applications, 1st ed., betz-druck GmbH, Darmstadt, 2003.

[2]. A. Momeni, S.M. Abbasi, Effect of hot working on flow behavior of Ti–6Al–4V alloy in single phase, *Mater. Des.* 31 (2010) 3599-3604.

[3]. X.G. Fan, H. Yang, P.F. Gao, Prediction of constitutive behavior and microstructure evolution in hot deformation of TA15 titanium alloy, *Mater. Des.* 51 (2013) 34-42.

[4]. H.Q. Liang, H.Z. Guo, Y. Nan, C. Qin, X.N. Peng, J.L. Zhang, The construction of constitutive model and identification of dynamic softening mechanism of high-temperature deformation, *Mater. Sci. Eng. A* 615 (2014) 42-50.

[5]. F.S. Qu, Y.H. Zhou, L.Y. Zhang, Z.H. Wang, J. Zhou, Research on hot deformation behavior of Ti–5Al–5Mo–5V–1Cr–1Fe alloy, *Mater. Des.* 69 (2015) 153-162.

[6]. J. Luo, M.Q. Li, X.L. Li, Y.P. Shi, Constitutive model for high temperature deformation of titanium alloys using internal state variables, *Mech. Mater.* 42 (2010) 157-165.

[7]. C. Li, X.Y. Zhang, K.C. Zhou, C.Q. Peng, Relationship between lamellar a evolution and flow behavior during isothermal deformation of Ti-5Al-5Mo-1Cr-1Fe near β titanium alloy, *Mater. Sci. Eng. A* 558 (2012) 668-674.

[8]. Y.Q. Ning, B.C. Xie, H.Q. Liang, H. Li, X.M. Yang, H.Z. Guo, Dynamic softening behavior of TC18 titanium alloy during hot, *Mater. Des.* 71 (2015) 68-77.

[9]. Q. Bai, J. Lin, T,A. Dean, D.S. Balint, T. Gao, Z. Zhang, Modelling of dominant softening mechanisms for Ti-6Al-4V, *Mater. Sci. Eng. A* 559 (2013) 352-358.

[10]. L.J. Huang, L. Geng, A.B. Li, X.P. Cui, H.Z. Li, G.S. Wang, Characteristics of hot compression behavior of Ti–6.5Al–3.5Mo–1.5Zr–0.3Si alloy with an equiaxed microstructure, *Mater. Sci. Eng. A* 505 (2009) 136-143.

[11]. J. Guo, L,F. Wang, S.F. Liu, M.Q. Li, The correlation between the flow behavior and the microstructure evolution during hot working of TC18 alloy, *Mater. Sci. Eng. A*

654 (2016) 213-220.
[12]. P.F. Gao, M. Zhen, X.G. Fan, Z.N. Lei, Y. Cai, Hot deformation behavior and microstructure evolution of TA15 titanium alloy with nonuniform microstructure, *Mater. Sci. Eng. A* 654 (2016) 213-220.
[13]. J. Lin, Y. Liu, T.A. Dean, A Review on damage mechanisms, models and calibration methods under various deformation conditions, *Int. J. Damage. Mech.* 14 (2005) 299-319.
[14]. R. Bobbili, V. Madhu, Flow and fracture characteristics of near alpha titanium alloy, *J. Alloy. Compd.* 684 (2016) 162-170.
[15]. M.S. Mohamed, A.D. Foster, J.G. Lin, D.S. Balint, T.A. Dean, Investigation of deformation and failure features in hot stamping of AA6082: Experimentation and modelling, *Int. J. Mech. Tool. Manuf.* 53 (2012) 27-38.
[16]. M.A. Khaleel, H.M. Zbib, E.A. Nyberg, Constitutive modeling of deformation and damage in superplastic materials, *Int. J. Plasticity.* 17 (2001) 277-296.
[17]. S.L. Semiatin, R.L. Goetz, E.B. Shell, V. Seetharaman, A.K. Ghosh, Cavitation and failure during hot forging of Ti-6Al-4V, *Metall. Mater. Trans. A* 30A (1998) 1411-1424.
[18]. S.L. Semiatin, V. Seetharaman, E.B. Shell, M.P. Simon, P.N. Fagin, Cavitation during hot tension testing of Ti–6Al–4V, *Mater. Sci. Eng. A* 256 (1998) 92-110.
[19]. X.J. Dong, S.Q. Lu, H. Z. Zheng, X. Li, D.L. Ouyang, Cavity nucleation during hot forging of Ti-6Al-2Zr-1Mo-1V alloy with colony alpha microstructure, Trans. *Nonferrous. Met. Soc. China.* 20 (2010) 2259-2264.
[20]. P.D. Nicolaou, R.L. Goetz, S.L. Semiatin, Influence of stress state on cavitation during hot working of Ti-6Al-4V, *Metall. Mater. Trans. A* 35A (654-662).
[21]. R. Bobbili, V. Madhu, Effect of strain rate and stress triaxiality on tensile behavior of titanium alloy Ti-10-2-3 at elevated temperatures, *Mater. Sci. Eng. A* 667 (2016) 33-41.
[22]. M.G. Cockcroft, D.J. Latham, Ductility and the workability of metals, *Journal of the Institute of Metals*. 96 (1968) 33-39.
[23]. D.Y. Seok, D. Kim, S.W. Kim, J. Bak, Y.S. Lee, K. Chung, Fracture criterion for AZ31 Mg alloy plate at elevated temperature, *Met. Mater. Int.* 21 (2015) 54-71.
[24]. G.R. Johnson, W.H. Cook, Fracture characteristics of three metals subjected to various strains, strain rates, temperature and pressures, *Eng. Fract. Mech.* 21 (1985) 31-48.
[25]. F.A. Mcclintock, A criterion for ductile fracture by the growth of holes, *J. Appl. Mech.* 35 (1968) 363-371.
[26]. M. Oyane, Criteria of ductile fracture strain, *Jsme. Int, J.* 15 (1972) 1507-1513.
[27]. J.R. Rice, D.M. Rracey, On the ductile enlargement of voids in triaxial stress fields, *J. Mech. Phys. Solids.* 17 (1969) 201-217.
[28]. A.L. Gurson, Continuum theory of ductile rupture by void nucleation and growth: Part I-yield criteria and flow rules for porous ductile media, *J. Eng. Mater.* 1 (1977) 2-15.
[29]. V. Tvergaard, A. Needleman, Analysis of the cup-cone fracture in a round tensile bar, *Acta Metall.* 32 (1984) 157-169.

[30]. V. Tvergaard, On localization in ductile materials containing spherical voids, *Int. J. Fracture.* 18 (1982) 237-252.

[31]. D.R. Hayhurst, M.T. Wong, F. Vakilitahami. The use of CDM analysis techniques in high temperature creep failure of welded structures, *Int. J. A-Solid. M.* 45 (2001) 90-97.

[32]. J. Lin, M Mohamed, D. Balint and T.A. Dean. The development of continuum damage mechanics-based theories for predicting forming limit diagrams for hot stamping applications, *Int. J. Damage. Mech.* 23 (2014) 684-701.

[33]. Y.M. Huo, J.G. Lin, Q. Bai, B.Y. Wang, X.F. Tang, H.C. Ji, Prediction of microstructure and ductile damage of a high-speed railway axle steel during cross wedge rolling, *J. Mater. Process. Tech.* 239 (2017) 359-369.

[34]. W.C. Xiao, B.Y. Wang, Y. Wu, X.M. Yang, Constitutive modeling of flow behavior and microstructure evolution of AA7075 in hot tensile deformation, *Mater. Sci. Eng. A* 721 (2018) 704-713.

[35]. L. Yang, B.Y. Wang, G. Liu, H.J. Zhao, W.C. Xiao, Behavior and modeling of flow softening and ductile damage evolution in hot forming of TA15 alloy sheets, *Mater. Des.* 85 (2015) 135-148.

[36]. J.L. Li, B.Y. Wang, H. Huang, S. Fang, P. Chen, J.X. Shen, Unified modelling of the flow behaviour and softening mechanism of aTC6 titanium alloy during hot deformation, *J. Alloy. Compd.* 748 (2018) 1031-1043.

[37]. G.Z. Quan, D.S. Wu, G.C. Luo, Y.F. Xia, J. Zhou, Q. Liu, L. Gao, Dynamic recrystallization kinetics in α phase of as-cast Ti-6Al-2Zr-1Mo-1V alloy during compression at different temperatures and strain rates, *Mater. Sci. Eng. A* 589 (2014) 23-33.

[38]. G.Z. Quan, G.C. Luo, J.T, Liang, D.S. Wu, A. Mao, Q. Liu, Modelling for the dynamic recrystallization evolution of Ti–6Al–4V alloy in two-phase temperature rage and a wide strain rate range, *Comp. Mater. Sci.* 97 (2015) 136-147.

[39]. W. Garrison. Ductile fracture. *J. Phys. Chem. Solids.* 48 (1987) 1035-1074.

[40]. J. Besson, Continuum models of ductile fracture: A review, *Int. J. Damage. Mech.* 19 (2010) 3-52.

[41]. J. Lemaitre, A continuous damage mechanics model for ductile fracture, *J. Eng. Mater-T. Asme.* 107 (1985) 83-89.

[42]. J. Lin, B.H. Cheong, X. Yao, Universal multi-objective function for optimising superplastic-damage constitutive equations, *J. Mater. Process. Tech.* 125 (2002) 199-205.

[43]. A.S. Khan, R. Kazmi, B. Farrokh, M. Zupan, Effect of oxygen content and microstructure on the thermos-mechanical response of three Ti-6Al-4V alloys: Experimental and modeling over a wide range of strain-rates and temperatures, *Int. J. Plasticity.* 23 (2007) 1105-1125.